DOI: 10.1111/cgf.12994

COMPUTER GRAPHICS *forum*
Volume 36 (2017), number 8 pp. 57–68

Virtual Inflation of the Cerebral Artery Wall for the Integrated Exploration of OCT and Histology Data

S. Glaßer[1], T. Hoffmann[2], A. Boese[3], S. Voß[4], T. Kalinski[5], M. Skalej[2] and B. Preim[1]

[1]Department of Simulation and Graphics, Otto-von-Guericke University, Magdeburg, Germany
{sylvia.glasser, bernhard.preim}@ovgu.de
[2]Institute of Neuroradiology, Otto-von-Guericke University, Magdeburg, Germany
t.hoffmann@ovgu.de, martin.skalej@med.ovgu.de
[3]Department of Medical Engineering, Otto-von-Guericke University, Magdeburg, Germany
axel.boese@ovgu.de
[4]Department of Fluid Dynamics and Technical Flows, Otto-von-Guericke University, Magdeburg, Germany
samuel.voss@ovgu.de
[5]Joint Practice for Pathology, Hamburg, Germany
kalinski@pathologie-hamburg.de

Abstract

Intravascular imaging provides new insights into the condition of vessel walls. This is crucial for cerebrovascular diseases including stroke and cerebral aneurysms, where it may present an important factor for indication of therapy. In this work, we provide new information of cerebral artery walls by combining ex vivo optical coherence tomography (OCT) imaging with histology data sets. To overcome the obstacles of deflated and collapsed vessels due to the missing blood pressure, the lack of co-alignment as well as the geometrical shape deformations due to catheter probing, we developed the new image processing method virtual inflation. We locally sample the vessel wall thickness based on the (deflated) vessel lumen border instead of the vessel's centerline. Our method is embedded in a multi-view framework where correspondences between OCT and histology can be highlighted via brushing and linking yielding OCT signal characteristics of the cerebral artery wall and its pathologies. Finally, we enrich the data views with a hierarchical clustering representation which is linked via virtual inflation and further supports the deduction of vessel wall pathologies.

Keywords:

ACM CCS: Categories and Subject Descriptors (according to ACM CCS): Computer Graphics [I.3.3]: Picture/Image Generation—Image Processing and Computer Vision [I.4]: Applications—Computer Applications [J.3]: Life and Medical Sciences

1. Introduction

With an increased rate of cerebrovascular diseases in the Western civilized countries, the need for an advanced vessel wall analysis increases as well. Usually, the contrast-enhanced vessel lumen data are acquired to provide information about possible vessel stenoses or pathologies such as cerebral aneurysms. However, the disease is often manifested in the vessel wall causing a pathologic weakening or thickening including arteriosclerotic plaque deposits. For clinical research, intravascular imaging, e.g., intravascular ultrasound (IVUS) and recently optical coherence tomography (OCT), provides new insights into the morphology of the wall and possible pathologic changes. IVUS and OCT are employed in clinical routine for cardiology to assess stenoses and plaques with superior image resolution compared to tomographic imaging. OCT data exhibit a spatial resolution of less than 15 μm with a limited penetration depth of 3–4 mm, whereas tomographic images are limited to 0.2 mm spatial resolution. Due to restrictions of the medical board, i.e., the catheters might not be small and flexible enough to guarantee a safe use in cerebral vessels in vivo, an adequate imaging modality for cerebral pathologic vessel wall changes is still missing.

© 2016 The Authors
Computer Graphics Forum © 2016 The Eurographics Association and John Wiley & Sons Ltd. Published by John Wiley & Sons Ltd.

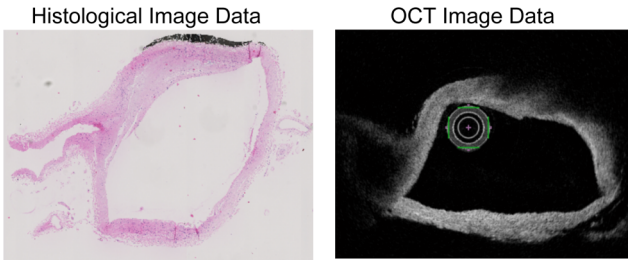

Figure 1: *Ex vivo histology and OCT slice depicting the same vessel part with varying shapes due to deflation.*

To assess the potential of characterizing cerebral arteriosclerotic plaque, OCT studies have been successfully carried out for the larger carotid arteries [YKYea12] as well as for animal studies or ex vivo studies [MSH*11]. Due to its ability to characterize pathological vessel wall changes and its spatial resolution superior to other intravascular imaging methods [TMF*12], it is expected that OCT imaging of the cerebral vessels will be employed and allowed for interventional use in the near future.

Our work focuses on the ex vivo evaluation of the Circle of Willis (CoW), the cerebral arterial circle that supplies the brain with blood. We correlate OCT imaging of the CoW containing plaque with histologic imaging. The combination is hampered by a deflation or collapse of the vessels due to the lack of an intact blood cycle (see Figure 1). Due to the CoW's numerous and particularly small branchings, a sufficient flushing is not applicable. Further changes of the vessel shape are caused by the ex vivo OCT catheter probing (small vessels are reshaped due to the catheter's size and stiffness) and by the sectioning of the preparations for histologic imaging. To overcome these limitations, we combine both image data modalities via virtual inflation.

The virtual inflation method is embedded in a multi-view framework for the interactive and simultaneous exploration of OCT and histology data. To assess the accuracy of the combination, we provide a quantitative evaluation based on a finite-element simulation creating a deformed virtual vessel wall model. Furthermore, we provide a clustering of the cell nuclei in the histological image data set for an adapted cluster visualization. We then combine the OCT characteristics via brushing and linking with the features extracted from histology. Finally, we transfer the cluster visualization to the OCT data and provide novel information about the vessel wall composition. This work is an extension of our previous work [GHB*15]. The additional contributions of this paper are:

- We extend the virtual inflation framework by combining it with a visual representation of clustered cell nuclei to allow for an improved evaluation of OCT image data. We are able to define and extract the spatial connectivity of the nuclei and identify and automatically derive important attributes for a dedicated visual representation. Thus, we can even transfer more information from the histologic data to the OCT image.
- Based on the newly available information, we provide medical findings which were extracted via combining OCT and histology.
- For an improved evaluation of our method, we refine previously developed virtual vessel phantoms and include a Poisson disk sampling for a quantitative evaluation.

2. Related Work

A lot of effort was spent in recent years on the visualization of vascular structures [OP05, AMB*13, KGPS13]. These methods focused on the visualization of vessel walls by means of polygonal meshes aiming at watertight surfaces, continuity and accuracy. For the visualization of vascular pathologies manifested in the vessel wall, these methods are not applicable. Direct volume rendering with appropriate transfer functions [GOH*10] enabled the simultaneous visualization of plaques, stents and vessel walls and thus, better serves diagnostic purposes. In contrast to the methods directly operating on tomographic radiological image data, we consider intravascular imaging.

An intravascular imaging-based evaluation of the arterial wall is mainly carried out in cardiology. Katouzian et al. [KKSea12] correlated IVUS with histological imaging. They created a cage fixture setup for an in vitro experiment. Also intended for the cardiological use, Balzani et al. [BBBea12] introduced a 3D reconstruction of geometrical models of arteriosclerotic arteries based on multimodal imaging including IVUS, virtual histology data and angiographic X-ray images. The reconstructed 3D model comprises the inner wall with color-coded parameters describing stress distributions, and a transparently rendered outer wall. In contrast, we are focusing on cerebral arteries. Thus, we deal with many particularly small vessel bifurcations yielding deflated vessels in the ex vivo imaging.

The analysis and the visualization of the vessel wall for cerebrovascular diseases, including aneurysms, is a novel research area, mainly motivated by intravascular imaging. In previous work, we prepared an artificial porcine aneurysm, probed it with IVUS and provided a visual representation of hemodynamic information as well as the wall thickness [GLH*14]. The flat map [NGB*09] visualized near wall flow data which is mapped onto the cerebral aneurysm surface. Instead of hemodynamic information, our virtual inflation method allows for the mapping of histological information onto the vessel wall.

Related to our analysis of the cerebral vessel wall, the curvicircular feature aggregation [MMVea13] samples information around the vessel's centerline to provide pathologic changes of blood vessels as an alternative to the curved planar reformation technique [KFW*02]. The curvicircular features allow for an expressive visualization of vessels and highlight stenoses. Born et al. [BSRea14] present the 2D stent map for aortic valve stenosis analysis, where generalized cylindric coordinates are extracted from the vessel centerline to create a mapping of different stent parameters, e.g., radial force or compression level. In contrast to these approaches, we do not sample around the vessel's centerline but rather along the inner vessel wall. Their work is also based on in vivo CT (angiography) imaging without deflated vessels. We developed the virtual inflation method to overcome the limitation of collapsing vessels, which is distantly related to the active contour and the balloon force concept [Coh91]. However, the active contour

© 2016 The Authors
Computer Graphics Forum © 2016 The Eurographics Association and John Wiley & Sons Ltd.

is allowed to move, i.e., it is attracted towards features such as edges. Our approach assumes a fixed length of the contour.

Similar to our work, virtual inflation can be applied to organic tissue instead of blood vessels. Such approaches were developed for endoscopic views, where a virtual view is generated from a tomographic image data set. Bartrolí et al. [BWKG01] introduced a virtual colon unfolding based on nonlinear ray casting and a nonlinear 2D scaling algorithm. The latter compensates distortions due to the unfolding of the colon similar to the nonlinear magnification fields used in information visualization. Hong et al. [HGQ*06] presented the conformal virtual colon flattening including a topological denoising to cope with high genus surface meshes. Zeng et al. [ZMG*10] applied a harmonic map registration to the conformal virtual colon flattened images to co-register supine and prone colon. Furthermore, the landmark-driven optimal quasiconformal mapping presented in [ZY14] straightens the main anatomical landmark curves of the colon. For future work, an adaption for the whole vessel, i.e., a virtual vessel flattening would be interesting.

Also related to our method is the medial axes approach, which can be applied to measure the thickness of medical structures, e.g., the corpus callosum [HKW12]. In contrast, we focus on a thickness measurement originating at the inner vessel wall and directed to the outer vessel wall.

The evaluation of hematoxylin and eosin (H&E) stained data is the standard method in histopathology and enables the pathologist to recognize tissue alterations, e.g., diagnosis and grading of cancer. Major trends for nuclei detection, segmentation, feature computation and classification techniques in digital histology data were presented in the exhaustive overview by Irshad et al. [IVRR14]. For the delineation of touching nuclei, the watershed approach has been successfully adapted for H&E data [LSP03, AM12]. Sertel et al. [SCSG09] also applied the watershed algorithm and reduced staining variations with anisotropic diffusion. Naik et al. [NDA*08] automatically segmented nuclear and glandular structures in H&E data based on three information levels: low-level information based on pixels, high-level information based on relationships between pixels for object detection and domain-specific information based on relationships between histological structures. Our approach includes pixel information as well as high-level information such that a neighborhood for each nucleus is determined and integrated in the clustering. For a more general system dealing with various histologically stained image data, Kårsnäs et al. [KSD*15] provided a comprehensive software tool for extracting and quantifying sub-cellular data. They especially account for biological and staining-induced variations.

Multi-view frameworks are often employed in medical visualization and analysis for data exploration [GRW*00]. Our prototype comprises two synchronized views of the cerebral vessels in a multi-view framework. Our work includes brushing and linking, a concept that was initially developed for highlighting data in scatterplots [BC87], to combine both views.

3. Image Data Acquisition

This section explains the image acquisition of the OCT data sets. Afterwards, the histology-based data sets are described.

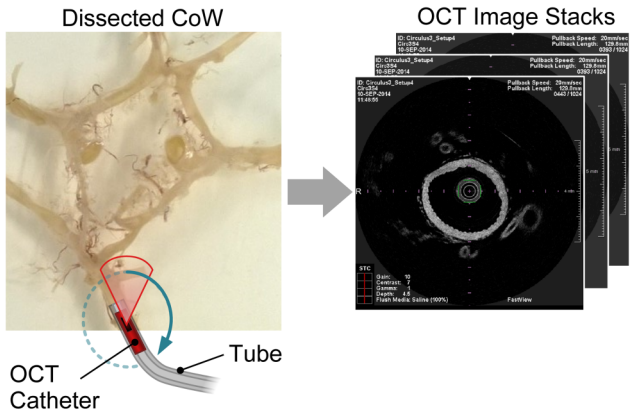

Figure 2: *Illustration of the intravascular OCT image acquisition based on the post-mortem dissected CoWs preparation yielding the 2D OCT image stacks.*

3.1. OCT image acquisition

Three human CoWs were explanted post-mortem, fixated with formalin and probed with OCT aiming at the characterization of vascular wall structures (see Figure 2). All investigations were performed in accordance with the local ethics committee. The specimens were examined for pathological changes of the vessel wall, e.g., plaque and aneurysms. The CoW preparations were flushed with isotonic saline solution. They were fixated with needles on a silicon pad in a container filled with saline solution for OCT image acquisition with a TERUMO LUNAWAVE^{TM} console (Terumo Corporation, Shibuya, Japan). The system is equipped with a near infrared laser light source in the spectral domain. The OCT system's pullback speed was 20 mm/s over an average distance of 130 mm yielding 1,024 slices with a pixel resolution of 15 μm $\times$ 15 μm.

During image acquisition, a constant saline flush of the CoW was started with an injector system. It reduced the deflation of the vessels, but it could not be prevented completely due to small outlets of the circle. Since only parts of the CoW could be acquired with one setup, i.e., with one placement of the OCT catheter, different OCT imaging setups were carried out for each preparation. As a result, we obtain a set of OCT image series for each vessel part of the CoW that exhibits vessel diameters large enough for catheter probing. Further information of the OCT imaging setup can be found in [GHB*15, HGBea16].

3.2. Histologic image acquisition

To assess vessel wall pathologies, we select certain vessel parts with arteriosclerotic plaque as well as prominent bifurcations for orientation purposes (see Figure 3). Additionally, the specimen was marked lengthwise doublesided with black and red ink. After paraffin embedding, cross-sections of the specimen were cut using a microtome with a thickness of 2 μm and a slice gap of 50 μm. The sections were transferred to standard glass slides, H&E stained and coverslipped. The slides were digitized using a Hamamatsu Nanozoomer (Hamamatsu Photonics, Hamamatsu, Japan) with a resolution of .23 μm per pixel. The original proprietary file was formatted to

© 2016 The Authors
Computer Graphics Forum © 2016 The Eurographics Association and John Wiley & Sons Ltd.

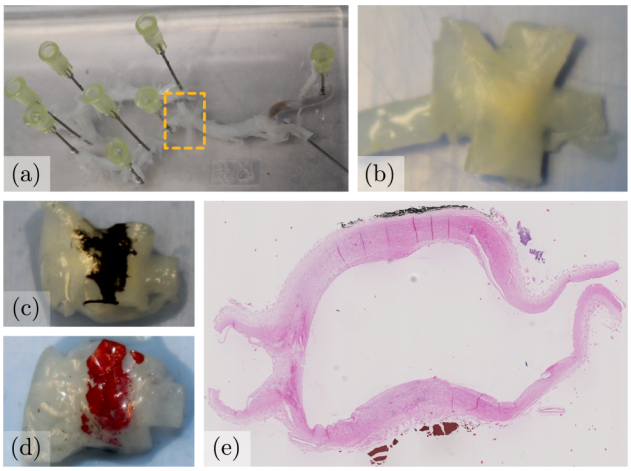

Figure 3: *From a dissected CoW (a), a specimen was taken, see inlet (b). Black and red ink is employed for later co-registration with OCT data (c and d). In the digitized H&E stained slice the red and black ink is still visible (e).*

JPEG2000 [KZSea08] and stacked into a volume for the processing with our framework. The original data comprise approx. 11,000 × 8,000 pixels per slice with a resolution of .92 μm per pixel.

4. Virtual Inflation for the Combined Evaluation of OCT and Histology Data

In this section, we describe our workflow (see Figure 4),. starting with the virtual inflation method. Afterwards, the clustering of the nuclei and our framework are presented.

4.1. Virtual inflation

The virtual inflation method allows for the inflation of deflated vessels. It can be applied to OCT and histology data since only the contours of the vessel walls are required. The process is subdivided in three steps (see Figure 4a).

Step 1: Extraction of equidistantly sampled contours. First, the contours of the vessel lumen, i.e., the inner wall, and the vessel-surrounding border, i.e., the outer wall, are required. We use manually segmented binary masks and process each wall separately. From the binary mask, all foreground pixels are selected forming a point set. Then, an arbitrary starting point is chosen and its closest, yet not visited, point is iteratively added to obtain a sorted list of contour points. Next, the list is equidistantly resampled. The amount of sample points is a user-defined parameter. Empirically determined default values are 400 for an OCT slice with 600 × 600 pixels and 1,600 for a histology slice with approx. 11,000 × 8,000 pixels. The overall length of the contour is divided by the number of sampling points yielding a contour segment length. Then, new sampling points are extracted as intersection points with the connected contour list such that the distance between two subsequent sample points equals the contour segment length.

Step 2: Extraction of normals and wall thickness. For each point p_i of the inner vessel wall, the normal vector $\overrightarrow{n_i}$ perpendicular to the line spanned by p_{i-1} and p_{i+1} is extracted (see Figure 4a). The normals are iteratively averaged as long as they intersect each other. We approximate the wall thickness t_i at p_i as distance to the outer wall by intersecting it with a ray originating at p_i in direction $\overrightarrow{n_i}$.

Step 3: Transformation of vessel walls and sampling of intensities. We virtually inflate the inner wall by projecting the k equidistantly sampled inner wall points p onto a circle with center m and radius r. Hence, m equals the mean of the points p. We extract $r = c/(2\pi)$, where c is the circumference of the inner wall. Approximating p_i' via:

$$p_i' = m + r \cdot \begin{pmatrix} \cos\alpha_i \\ \sin\alpha_i \end{pmatrix} \tag{1}$$

ensures equidistant points onto the circle, where $\alpha_i = i * 2\pi/n$ and $i = [1, k]$. We remodel the outer wall by adding the stored values for t_i to p_i' in the direction $\overrightarrow{mp_i}'$. As a result, we obtain the virtually inflated vessel walls. With linear interpolation, we can create intermediate steps. For example, we translate the point p_i only half the distance between p_i and p_i' of the virtually inflated circular inner vessel wall (see the illustration for *Step 3* in Figure 4a). The interpolated virtual inflation is presented in Figure 5. It allows the clinical expert an interactive inflation and exploration of the data. The transition from original data to virtually inflated data can be visualized in an animated manner, as well. The user defines how many intermediate stages should be created. For the translation of intensity values from the original image data to the virtually inflated image, the rays $\overrightarrow{n_i}$ are sampled (see Figure 6). We acquire a list of samples for each pixel of the virtual inflated images (if k rays cover the pixel, then k samples are obtained) and interpolate the pixel's intensity by averaging over the samples. If a pixel x with no samples exists, the pixel's intensity value $I(x)$ is interpolated from its neighborhood N (see Figure 6c):

$$I(x) = \sum_{q}^{q \in N} \frac{1}{w_q} * I(q). \tag{2}$$

The sum of weights $\sum w$ drops below 1 if more than one pixel is missing. In this case, we leave the missing pixels out and divide the sum of the remaining pixels by $\sum w$. To exploit as many samples as possible, we first create a ranking of the pixels, based on their number of missing neighbors. Then, we interpolate all pixels with one neighbor missing, followed by pixels with two neighbors missing and so on. The interpolation is restricted to vessel wall pixels with a point-in-polygon test based on the two walls. We empirically set the step size for the sampling to .2 of the pixel's width. Larger step size values would gather less samples with more missing pixels. Smaller values would result in more samples per pixel and slightly increased computation time.

The runtime of the virtual inflation step depends on the number of intermediate images. For the presented OCT data, the sampled

© 2016 The Authors
Computer Graphics Forum © 2016 The Eurographics Association and John Wiley & Sons Ltd.

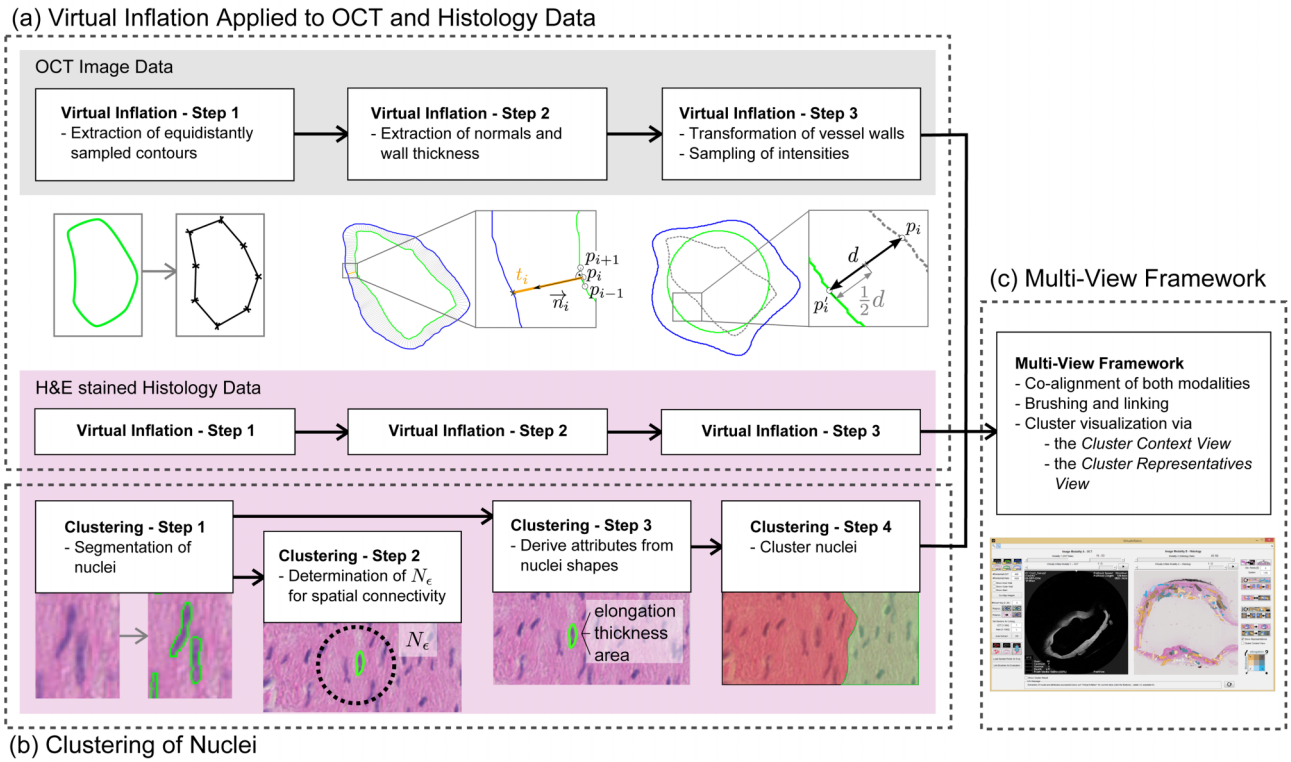

Figure 4: *Illustration of the proposed framework for exploration of the cerebral vessel wall with virtual inflation. The virtual inflation of the OCT image data is depicted which comprises three steps (a). These steps are repeated for the histology data. The four steps for clustering the histology data are depicted at the bottom (b). The virtually inflated images of OCT and histology data as well as the clustering result serve as input for the interactive exploration within our multi-view framework (c). It allows for co-alignment of both modalities as well as brushing and linking, which can be further combined with the cluster context view or the cluster representatives view.*

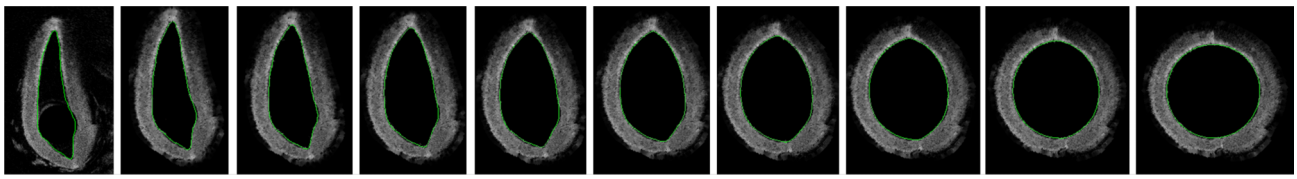

Figure 5: *Result (right) of the virtual inflation and the sampling of intensity values applied to a deflated vessel OCT cross-section view (left). Intermediate steps are based on the linearly interpolated inner vessel wall points.*

intensities are extracted in .5 s. The creation of the single virtually inflated circular cross-section from the sampled intensities costs 3.7 s whereas the creation of 10 intermediate images costs 35.4 s on a desktop PC with 8 GB RAM and an Intel(R) Core i5 CPU (3.20 GHz).

4.2. Hierarchical clustering of nuclei

For the evaluation of vessel wall pathologies, the most important information extracted from the H&E stained histological image data comprises the presence, arrangement and shape of nuclei. The nuclei shape allows for a rough classification of cell types, e.g., elongated nuclei often correspond to mesenchymal cells. Inflammations are characterized by infiltrates of different types of cells, e.g., lymphocytes with small round nuclei. The clinical expert also takes additional information into account, e.g., composition of the walls by analyzing tissue types. Based on discussions with our pathological cooperation partners, we decided to focus on cell nuclei with round and elongated shapes. A further requirement was the clustering of similar, spatially connected nuclei and thus, to provide a quick overview representation. Therefore, we developed an extraction of clusters (recall the clustering steps depicted in Figure 4b).

Step 1: Segmentation of nuclei. For the nuclei segmentation, we convert the colored H&E stained histology image into a gray image and invert it subsequently. To account for variations of intensities

© 2016 The Authors
Computer Graphics Forum © 2016 The Eurographics Association and John Wiley & Sons Ltd.

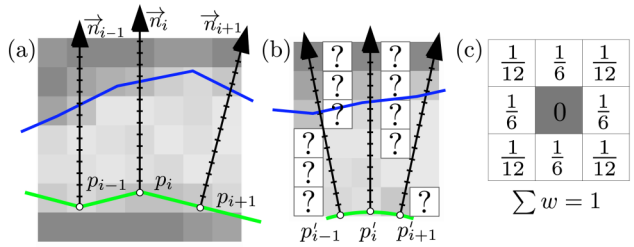

Figure 6: *Illustration of intensity value sampling. Depiction of the original image with the inner (green) and outer (blue) vessel wall (a). The samples are accumulated along the rays to interpolate values (b). If no sample value was assigned, the intensity is interpolated with the depicted filter (c).*

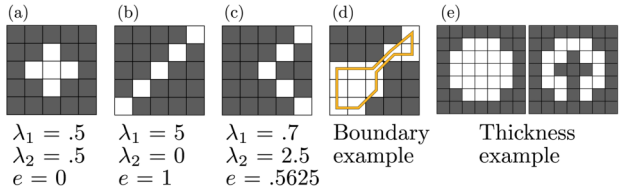

Figure 7: *Examples of segmented nuclei pixels and their elongation e (a–c). Next, a pixel set with its boundary (orange) is presented (d). Two pixel sets are shown yielding similar values for e but with distinct thickness values (e).*

and colors due to scanning, non-uniform illumination and staining, we apply a contrast-limited adaptive histogram equalization which works on small regions rather than on the entire image [Zui94]. Next, we automatically separate the nuclei from the background with Otsu's method [Ots79] which calculates an optimal threshold by minimizing the intraclass variances of the foreground and background class. Foreground objects smaller than ten pixels are removed. As suggested in [SCSG09], we apply anisotropic diffusion filtering [PM90] to smooth the histologic image data while preserving the edge information. Finally, we apply the watershed transform for a delineation of nuclei. This approach defines a group of basins in the image domain such that ridges in between these basins can be employed as borders to isolate the nuclei from each other. Based on the borders, a binary mask is created which holds the estimated boundaries for the nuclei.

Step 2: Determination of spatial connectivity. We determine the position of each nucleus as mean of the associated pixels' positions. Next, we approximate a neighborhood size N_ϵ for the nuclei depending on a user-defined minimum number of neighbors *MinPoints*. Here, a default value of 5 yields suitable results for all tested histological data sets. We build the k-distances graph (also called elbow function) for the given *MinPoints* value, as suggested in [EKSX96]. The graph maps the distance of each nucleus to its k next neighbors (with $k = MinPoints$). A well-suited N_ϵ can be automatically detected at the elbow point. Nuclei with an Euclidean distance smaller than N_ϵ are neighbored.

Step 3: Extraction of attributes from nuclei shapes. We want to differentiate between long, elongated nuclei and smaller, round nuclei, e.g., from inflammatory cells. Therefore, we derive the following attributes (see Figure 7):

- the *elongation* is a customized parameter for characterization of the roundness of the nucleus,
- the *thickness* describes the nucleus' thickness, i.e., the number of erosion steps (with a 3×3 rectangular kernel element) necessary to completely remove the object, and
- the *area* describes the nucleus' size, i.e., the number of pixels.

We extract the *elongation* e with a principal component analysis and subsequent evaluation of the eigenvalues λ_1 and λ_2 (see Figure 7). We normalize λ_1 and λ_2 with $l_1 = \lambda_1/(\lambda_1 + \lambda_2)$, $l_2 = \lambda_2/(\lambda_1 + \lambda_2)$ and extract e:

$$e = \max(l_1, l_2) - \min(l_1, l_2) \tag{3}$$

The main advantage of this measure compared to more conventional parameters, such as compactness, is its direct extraction and robustness. Since nuclei pixel positions are stored as binary masks, we do not have round shapes or smooth boundaries. Hence, a time-consuming extraction of the required information, e.g., the perimeter, the minimum bounding box or the longest chord, would be necessary. Especially if the pixel masks are incomplete due to noise, our *elongation* measure yields satisfying results. In case of round nuclei, we can separate round shapes from curved objects with the thickness parameter (see Figure 7e).

Step 4: Clustering of nuclei. We employ an agglomerative hierarchical clustering. Similar to region merging, each nucleus is forming its own cluster at the beginning. Each cluster is neighbored to clusters of corresponding nuclei within the distance N_ϵ. Then, the most similar neighbored clusters are merged into a new cluster and the neighbor list is built up from the merged clusters. The similarity is defined as Euclidean distance between the feature vectors, where each cluster has a feature vector that contains the mean values of the cluster pixel's attributes. Prior to clustering, z-scoring is applied to each attribute. From the cluster hierarchy we obtain cluster results based on two parameters: the minimum cluster size and the ϵ-value that defines the cluster division. We substitute the first one with the *MinPoints* parameter, since the spatial connectivity is already adapted to this value. The ϵ-value is empirically set to 1.0, but can be adapted to obtain a coarser or finer cluster division.

4.3. Framework

First, we describe the multi-view framework and second, we explain the included cluster views.

The multi-view framework. The virtual inflation and the clustering are combined into a multi-view framework implemented in MATLAB (MathWorks, Natick, USA) for the interactive exploration of the OCT and histological data (recall Figure 4c). The implementation is sped up by using vectorized data structures leveraging MATLAB's implicit multithreading capabilities as well as explicit parallel computing techniques and GPU computing. The

© 2016 The Authors
Computer Graphics Forum © 2016 The Eurographics Association and John Wiley & Sons Ltd.

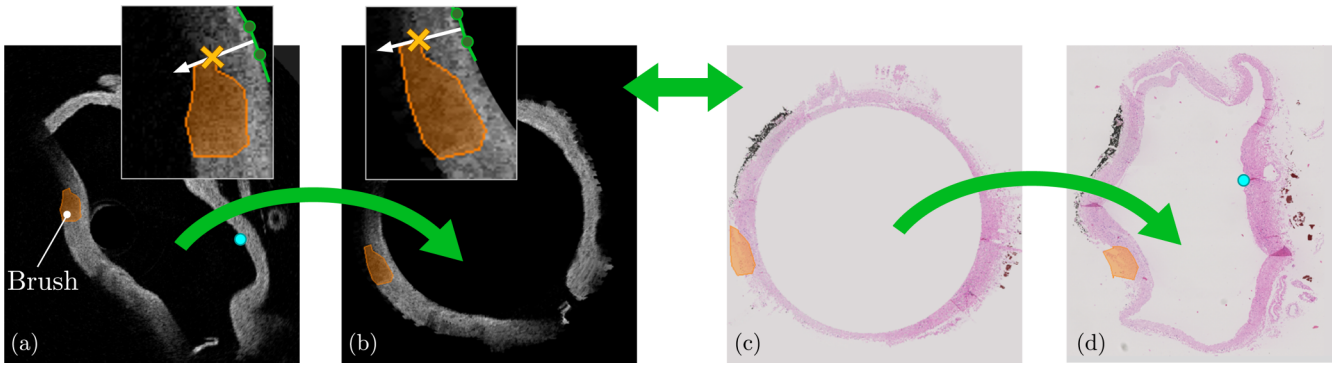

Figure 8: *Illustration of brushing and linking. Corresponding OCT and histology slices and their virtually inflated images are depicted. When the user defines a brush (a), it is automatically converted to the inflated view (b), based on the distance of the vertices of the brush and their distance to the vessel-lumen border (see inlets). The virtually inflated images of OCT and histology can be correlated (b and c). Analogously, the brush can be translated from the inflated to the original image (d).*

gpuArray command transfers data to the GPU memory. Subsequent image processing methods are performed on the GPU and the results are transferred back using the *gather* command. Furthermore, the *parfor* command distributes independent loop iterations across multiple MATLAB sessions using a multi-core CPU.

An initial correlation of the vessels is carried out with two landmarks, e.g., a vessel bifurcation, to determine a corresponding slice in both modalities. Next, the data sets are co-aligned based on the known slice distance of the OCT and histology data. If the user scrolls to a slice in one view, the other view is updated accordingly. For inspection of the data, virtual inflation is separately carried out for the OCT image data and the H&E stained histology data (recall Figure 4a). The user can qualitatively explore the vessel wall and choose between different interpolation steps (see Figure 5). Thus, the clinician can work with an intermediate image instead of the virtually inflated one.

Based on the virtual inflation results, our framework allows for brushing and linking for an interactive exploration (see Figure 8). The user selects a set of points forming a polygonal region of interest (ROI) – the brush. This brush is translated for each interpolation step of the virtual inflation. Finally, a correlation between a brush from the virtually inflated OCT image to the virtually inflated histology image (or vice versa) is carried out. As a prerequisite, the user selects two corresponding landmarks on the inner vessel wall of the virtually inflated images, e.g., the small vessels (see cyan circles) in Figure 8. The brush from the virtually inflated histology image is translated to the original histology image. Thus, an ROI defined in the original OCT image will be linked to its corresponding ROI in the original histology image (or vice versa). The clinician can correlate the image characteristics of a specific vessel wall part. Our collaboration partners preferred the evaluation in the original images by restricting the histology information to the brush.

The cluster views. We included two cluster views in our framework: a color coding of the clusters for context information – *the cluster context view* – and the adapted visualization of the cluster representatives – *the cluster representatives view*.

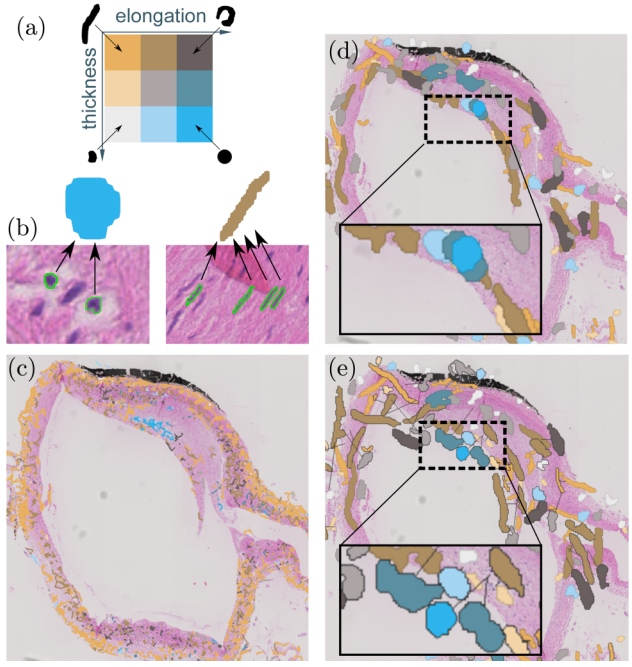

Figure 9: *The bivariate colormap is used for the color-coding of clusters (a). Examples of two clusters and their cluster representatives (b). The cluster context view provides context information but visual clutter as well (c). The cluster representatives view yields a sparse visualization (d), which will be further improved with the adjusted positions (e).*

The cluster context view maps the cluster average attributes (i.e., the average attributes of all cluster elements) to color with a bivariate color map (see Figures 9a–c). We employ orange and blue to achieve a visual separation from the H&E stained image data. The complementary colors work with red-green color blindness and allow for an intuitive highlighting of the different shaped nuclei.

© 2016 The Authors
Computer Graphics Forum © 2016 The Eurographics Association and John Wiley & Sons Ltd.

For all segmented nuclei positions, we carry out a Delaunay triangulation. Next, we identify inner triangles, i.e., triangles connecting only nuclei included in the cluster. In addition, edges of the Delaunay triangulation which do not belong to inner triangles but are spanned between two cluster elements, are selected. Inner triangles and the selected edges are color-coded (see Figure 9c). To avoid visual clutter, the cluster context visualization can be switched off and replaced by the cluster representatives view (see Figure 9d).

The cluster representatives view shows color-coded glyphs representing the cluster attributes inspired by choropleth maps. For the initial positioning, we employ the position of the most likely cluster element compared to the cluster's attributes. For the extraction of the glyph's shape, we transfer the assigned pixel map of the most likely cluster element into a polygon and slightly smooth the polygon's outline. We employ the bivariate color map and add a silhouette with a slightly darkened color for an improved visual separation from the remaining image. These glyphs are enlarged and mapped at the cluster representatives' positions.

Cluster representatives may overlap which hampers the visualization result (see Figure 9d). Since the overlap-free positioning problem of these cluster representatives is not deterministically solvable in polynomial time (NP-hard) [MS93], we developed a fast approximation consuming only a few seconds. We use an image buffer with reduced size for the adaption of cluster representatives' positions. For the employed histological data, we achieved satisfying results with a reduction factor of 1/30 yielding an image buffer of 370 × 300 pixels. Then, we mask the corresponding pixels of the downscaled cluster representatives at its initial position in the image buffer. If no overlap occurs, we store this position and proceed with the next cluster. Otherwise, we move the pixel mask in the image buffer one pixel to the left, right, top, and bottom yielding four altered image buffers. Then, we select the image buffer where the Haussdorff distance to the original position increased and the smallest amount of overlapping pixels occurs. This prevents cyclic translations. We repeat this procedure until no pixels overlap and store the translation. In peripheral areas, no valid position may be found due to limited space. Hence, we stop the rearrangement of the current cluster representative, if we reach the image buffer's boundaries or if the current translation exceeds a previously defined threshold (e.g., a Hausdorff distance of 100 pixels in the image buffer). In this case, we place the cluster representative at its original position, accepting an overlap. In Figure 9e, the adapted cluster representatives' positions are presented. Lines connect adjusted cluster representatives to their initial position in the original image (see inlets of Figures 9d and e).

When employing the cluster result as brush, the clusters can be linked to the OCT view. Therefore, the set of nuclei and their positions are interpreted as points of the polygonal brush and transferred to the OCT data. Furthermore, the cluster view can be restricted to clusters covered by the polygonal brush.

5. Evaluation

Our method is tailored to deflated vessels in OCT and histology data. Due to the novelty of the medical application, a ground truth is not available. To overcome this limitation, we designed a software phantom (see Figure 10a), and applied two deformation configurations via finite-element simulations yielding detailed positions and displacements of the discrete elements. The finite-element method is widely used to numerically simulate the relation of deformation, mechanical strain and stress, based on the conservation of the momentum, which is solved locally for each finite element. Based on this, we can conduct an evaluation taking into account the material behavior in combination with known locations of each discrete element. The static simulations considering large deflections and small strains were carried out with ANSYS Mechanical (ANSYS, Inc., Canonsburg, USA).

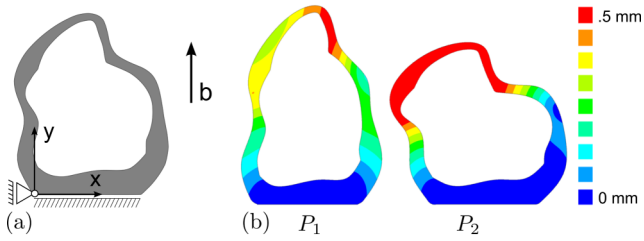

Figure 10: *Depiction of the software phantom in the initial, stress-free state (a). The local coordinate system is shown at the bottom. The application of the load b yields P_1 and P_2, while the bottom is fixated to prevent rigid body motion. Contour plots of the vector displacement magnitudes for software phantoms P_1 and P_2 (b).*

The initial 2D model with a circular cross-section [GHB*15] was extended to a more realistic one. The dimensions are carefully matched to the properties of cerebral vessels, with an inner radius of 2.2 mm and a heterogeneous vessel wall of .3 mm. The wall thickness variations serve as anatomical landmarks for the virtual inflation step. The numerical model consists of 96,000 tetrahedral elements with quadratic basis functions to obtain high accuracy. To induce deformation, a load b is applied as body force in positive and negative y-coordinate direction, yielding the software phantoms P_1 and P_2, see Figure 10b). Fixating the displacement in y-direction at the bottom edge and in x-direction at the bottom left vertex prevents rigid body motion. The load causes mechanical stress in the model's inside and results in deformation depending on the specified linear elastic material model. For investigation of the movement of the cerebral vessel walls, the Young's modulus is 1 MPa, the Poisson's ratio is 0.45 and the density is 1,000 kg/m^3 [BHZea10].

The displacement of P_1 and P_2 ranges up to .5 mm. P_1 and P_2 consist of 195,000 indexed vertices, where the world coordinates and displacements for each vertex are stored and employed as ground truth. We build two DICOM files based on P_1 and P_2. We employ an image size of 500 × 500 pixels, where 1 pixel covers .01 mm × .01 mm. The x-coordinates of P_1 range from -.26 mm to 3.00 mm and the y-coordinates from 0 mm to 4.62 mm. For P_2, x-coordinates range from -.96 mm to 3.15 mm and y-coordinates from -.01 mm to 3.76 mm. We extract for each vertex of P_1 and P_2 its pixel position by translating the origin in the bottom left of the bounding box yielding the images I_1 and I_2.

We load I_1 and I_2 into our framework and carry out brushing and linking. Originally, we brushed 3 polygons as well as a random

© 2016 The Authors
Computer Graphics Forum © 2016 The Eurographics Association and John Wiley & Sons Ltd.

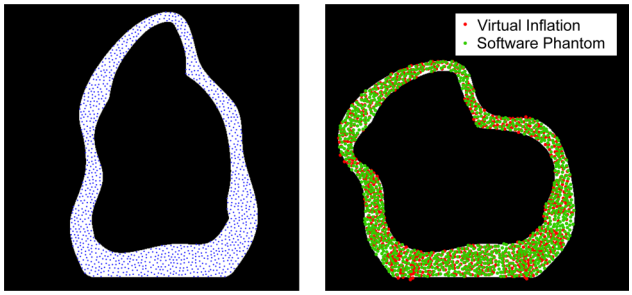

Figure 11: *Depiction of the binarized images I_1 and I_2 and the Poisson disk sample set. Via virtual inflation followed by brushing and linking, the corresponding positions (red) were extracted and compared with the ground truth (green).*

point set comprising 100 points to compare the virtual inflation results with the ground truth [GHB*15]. However, some of the randomly placed points were too tightly packed together or too sparsely distributed. We improved this quantitative evaluation by scattering 1,000 points which are Poisson disk sampled on the foreground object of I_1 forming our sample set, see Figure 11. Therefore, we adapted the approach in [Tul08], which is based on [Bri07]. With the Poisson disk sampling, a more homogeneously scanning of the vessel wall is ensured.

For the quantification of displacement errors induced by the virtual inflation, we compare the pixel coordinates of the corresponding brushes obtained via brushing and linking with the coordinates directly extracted from P_1 and P_2. Therefore, we carry out the following steps:

1. Extract the pixel coordinates for each sample point in I_1.
2. Select the corresponding world coordinates of P_1, i.e., transpose the pixel coordinates into world coordinates.
3. Derive the corresponding world coordinates of these vertices in P_2 (known from the finite-element simulation).
4. Convert the vertices from P_2 into pixel coordinates of I_2.
5. Compare these pixel coordinates with the pixel coordinates from I_2 extracted via brushing and linking.

The resulting average displacement of the sample set compared to the ground truth is 61.94 μm. This error is slightly larger than for the initial, more circle-like software phantom [GHB*15]. Reasons might be the more complex phantom as well as Poisson disk sampling that yields many points close to the border of the outer vessel wall. However, the result is satisfying. In relation to the image size of 500×500 pixels, the displacement of 6.19 pixels equals 1.24 %. Although the small displacement rate depends on the perfectly matched software phantom and may differ for real preparations, the virtual inflation allows for linking of a defined brush in one image to the other image.

6. Medical Findings

We applied the virtual inflation to several OCT data sets of the CoW and their corresponding histological images, including the basilar artery with arteriosclerotic plaque. We discussed the results with a neuroradiologist and a pathologist and provide the most important findings in Figure 12.

In Figure 12a, the histologic evaluation revealed a fibrotic plaque deposit in the pathologically thickened intima, i.e., the inner vessel wall layer. When brushing the deposits, the linking to the OCT slice reveals an area with dense plaque accumulation, see the dense tissue parts with high attenuation (marked with *) yielding the low attenuated areas behind. These findings are reflected by the clustering with blueish, circular shaped cluster representatives indicating inflammatory areas compared to orange-colored cluster representatives in healthy tissue.

In Figure 12b, the brush covers an accumulation of mucoid plaque, which is typically loose. As it can be seen in the OCT image, the brushed region is part of the plaque area with low signal and low attenuation, but no specific differences can be extracted. The cluster view restricted to the brush in the histology image does not highlight any conspicuous nuclei shapes.

In Figure 12c, a small area with inflammatory cells, characterized by sharp, round cell nuclei, was selected. Inflammations often vary and a precise prediction concerning their density values is not possible. This is reflected in the small brush in the OCT image (Figure 12c, right), which reveals a small, heterogeneous area. Hence, the cluster view, restricted to the brush that was linked to the OCT image, comprises a sharp, round, blueish nucleus shape as well.

The brush in Figure 12d covers a part of the vessel wall which was conspicuous during histology evaluation due to its increased thickness. However, the analysis of the histologic image does not confirm a plaque deposit. Probably, this area is caused by a cutting artifact. In accordance, no change in the signal characteristics of the OCT data occurs. This is also reflected by the clustering view that is restricted to the brush. Hence, it does not contain any conspicuous nuclei shapes.

The virtual inflation correlates the fibrotic plaque deposit to a homogeneous signal-rich region in the OCT data which matches findings in literature [KBBea06]. In case the vessels exhibit ellipsoidal cross-sections as well as various elongated cross-sections due to pathologies, an evaluation of the slightly virtually inflated vessel was beneficial, recall Figure 5.

7. Discussion

The proposed virtual inflation supports a combined analysis of OCT and histologic image data. The spatial differences between a brush and the corresponding brush in the second modality were evaluated based on finite-element simulations yielding a sufficient precision. For the medical image data, the co-alignment could be further improved by implanting some markers, e.g., a small thread, in the preparations. Our data sets were probed ex vivo. Thus, a detachment of the intima emerged, which typically occurs during decomposition. Hence, a larger study could provide more information about artifacts such as conservation-based shrinking.

The pathologic expert rated the cluster primitives, especially their accordance with the underlying morphologic features, as very useful extension for a quick overview of nuclei shapes especially in the OCT slices. Once an interesting vessel part was detected, the

© 2016 The Authors
Computer Graphics Forum © 2016 The Eurographics Association and John Wiley & Sons Ltd.

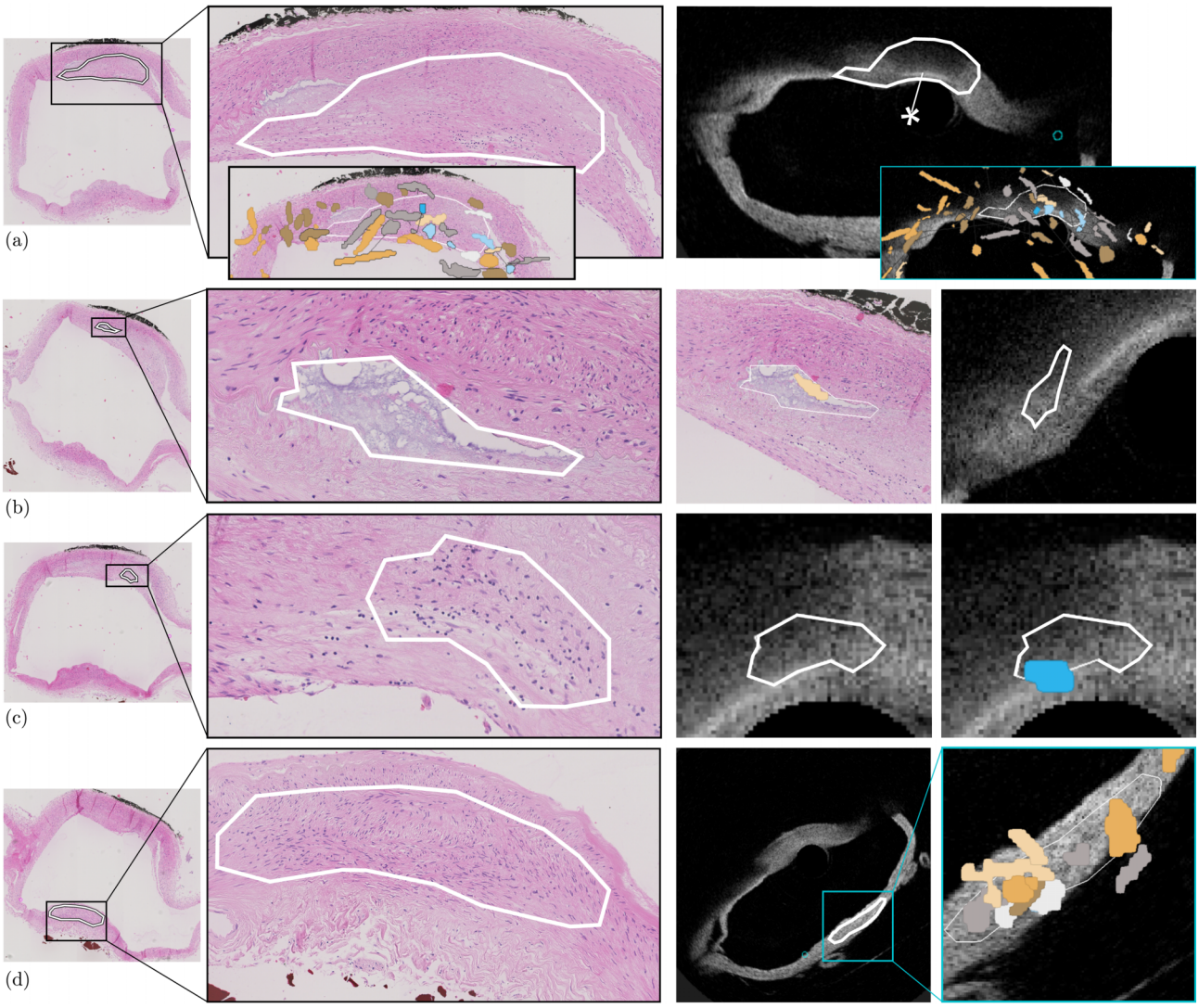

Figure 12: *Examples for the correlation of histology and OCT images. For each example (a–d), the left and second from left columns represent the histologic image including an enlarged view of pathologies. Brushes were defined in the histologic view and linked to the OCT view via virtual inflation. The cluster representatives are shown for the whole vessel cross-sections (see inlays in a). The cluster view can be restricted to the histological brush (b), as well as to the linked brush in the OCT view (c and d).*

original histologic data set was evaluated for an in-depth analysis. The combination of the ex vivo OCT and histologic properties provides new information about the cerebral vessel wall morphology and its corresponding OCT imaging. Such findings can form the basis for a solely radiology-based OCT image evaluation.

8. Summary and Future Work

In this paper, we presented a virtual inflation of ex vivo vessel parts probed with OCT and acquired with histology to analyze characteristics of the cerebral vessel wall. Our prototype requires manual segmentation of the vessel-lumen and the vessel-surrounding borders. It is adapted to intravascular imaging of the cerebral vasculature. Our framework comprises multiple coordinated views, which allows for brushing and linking between the OCT image and the histological image. Our work provides basic information for the radiologic evaluation of OCT signal characteristics which are almost unknown for cerebral artery walls.

Future work should include automatically segmented vessel walls of the OCT data [TSDS*11]. We are also particularly interested in a setup similar to the cage fixture [KKSea12] for an in vitro setup. However, their work is based on IVUS, whereas OCT would require different adaptions. Also, an analytic representation of the inner vessel wall and the wall thickness values could be developed to avoid averaging steps and reduce the calculation time. Finally, our work has great importance for the fluid-structure interaction regarding vessel wall and blood flow. The new wall information based on virtually inflated images currently serves our cooperation

© 2016 The Authors
Computer Graphics Forum © 2016 The Eurographics Association and John Wiley & Sons Ltd.

partners to examine the effect of wall thickness on the hemodynamic simulation.

Acknowledgements

This work was partly funded by the German Federal Ministry of Education and Research within the Forschungscampus *STIMULATE* (grant number: 13GW0095A).

References

[AM12] Ali S., Madabhushi A.: An integrated region-, boundary-, shape-based active contour for multiple object overlap resolution in histological imagery. *IEEE Trans. Med. Imaging 31*, 7(2012), 1448–1460.

[AMB*13] Auzinger T., Mistelbauer G., Baclija I., Schernthaner R., Köchl A., Wimmer M., Gröller M. E., Bruckner S.: Vessel visualization using curved surface reformation. *IEEE Trans. Vis. Comput. Graph. 19*, 12 (2013), 2858–2867.

[BBBea12] Balzani D., Böse D., Brands D., et al.: Parallel simulation of patient-specific atherosclerotic arteries for the enhancement of intravascular ultrasound diagnostics. *Engineering Computations 29*, 8 (2012), 888–906.

[BC87] Becker R. A., Cleveland W. S.: Brushing scatterplots. *Technometrics 29*, 2 (1987), 127–142.

[BHZea10] Bazilevs Y., Hsu M.-C., Zhang Y., et al.: A fully-coupled fluid-structure interaction simulation of cerebral aneurysms. *Comput. Mech. 46*, 1 (2010), 3–16.

[Bri07] Bridson R.: Fast poisson disk sampling in arbitrary dimensions. In *ACM SIGGRAPH* (2007), p. 5.

[BSRea14] Born S., Sundermann S. H., Russ C., et al.: Stent maps - comparative visualization for the prediction of adverse events of transcatheter aortic valve implantations. *IEEE Trans. Vis. Comput. Graph. 20*, 12 (2014), 2704–2713.

[BWKG01] Bartrolí A. V., Wegenkittl R., König A., Gröller E.: Nonlinear virtual colon unfolding. In *Proc. of IEEE Visualization* (2001), pp. 411–420.

[Coh91] Cohen L. D.: On active contour models and balloons. *CVGIP: Image Understanding 53*, 2 (1991), 211–218.

[EKSX96] Ester M., Kriegel H.-P., Sander J., Xu X.: A density-based algorithm for discovering clusters in large spatial databases with noise. In *Proc. of Knowledge Discovery and Data Mining* (1996), pp. 226–231.

[GHB*15] Glasser S., Hoffmann T., Boese A., Voss S., Kalinski T., Skalej M., Preim B.: Histology-based evaluation of optical coherence tomographic charateristics of the cerebral artery wall via virtual inflating. In *Proc. of Eurographics Workshop on Visual Computing for Biology and Medicine (VCBM)* (2015), pp. 149–158.

[GLH*14] Glasser S., Lawonn K., Hoffmann T., Skalej M., Preim B.: Combined visualization of wall thickness and wall shear stress for the evaluation of aneurysms. *IEEE Trans. Vis. Comput. Graph. 20*, 12 (2014), 2506–2515.

[GOH*10] Glasser S., Oeltze S., Hennemuth A., Kubisch C., Mahnken A., Wilhelmsen S., Preim B.: Automatic transfer function specification for visual emphasis of coronary artery plaque. *Computer Graphics Forum 29*, 1 (2010), 191–201.

[GRW*00] Gresh D. L., Rogowitz B. E., Winslow R. L., Scollan D. F., Yung C.: WEAVE: A system for visually linking 3-d and statistical visualizations, applied to cardiac simulation and measurement data. In *Proc. of IEEE Visualization* (2000), pp. 489–492.

[HGBea16] Hoffmann T., Glasser S., Boese A., et al.: Experimental investigation of intravascular OCT for imaging of intracranial aneurysms. *Int. J. Comput. Assist. Radiol. Surg. 11*, 2 (2016), 231–241.

[HGQ*06] Hong W., Gu X., Qiu F., Jin M., Kaufman A.: Conformal virtual colon flattening. In *Proc. of the Symposium on Solid and Physical Modeling* (2006), pp. 85–93.

[HKW12] Herron T. J., Kang X., Woods D. L.: Automated measurement of the human corpus callosum using MRI. *PMC 25*, 6 (2012).

[IVRR14] Irshad H., Veillard A., Roux L., Racoceanu D.: Methods for nuclei detection, segmentation, and classification in digital histopathology: A review – current status and future potential. *IEEE Rev. Biomed. Eng. 7*, (2014), 97–114.

[KBBea06] Kawasaki M., Bouma B. E., Bressner J., et al.: Diagnostic accuracy of optical coherence tomography and integrated backscatter intravascular ultrasound images for tissue characterization of human coronary plaques. *Journal of the American College of Cardiology 48*, 1 (2006), 81–88.

[KFW*02] Kanitsar A., Fleischmann D., Wegenkittl R., Felkel P., Gröller M. E.: CPR: Curved planar reformation. In *Proc. of IEEE Visualization* (2002), pp. 37–44.

[KGPS13] Kretschmer J., Godenschwager C., Preim B., Stamminger M.: Interactive patient-specific vascular modeling with sweep surfaces. *IEEE Trans. Vis. Comput. Graph. 19*, 12 (2013), 2828–2837.

[KKSea12] Katouzian A., Karamalis A., Sheet D., et al.: Iterative self-organizing atherosclerotic tissue labeling in intravascular ultrasound images and comparison with virtual histology. *IEEE Trans. Biomed. Eng. 59*, 11 (2012), 3039–3049.

[KSD*15] Kårsnäs A., Strand R., Doré J., Ebstrup T., Lippert M., Bjerrum K.: A histopathological tool for quantification of biomarkers with sub-cellular resolution. *Computer Methods in Biomechanics and Biomedical Engineering: Imaging & Visualization 3*, 12015), 25–46.

© 2016 The Authors
Computer Graphics Forum © 2016 The Eurographics Association and John Wiley & Sons Ltd.

[KZSea08] KALINSKI T., ZWÖNITZER R., SEL S., et al.: Virtual 3D microscopy using multiplane whole slide images in diagnostic pathology. *American Journal of Clinical Pathology 130*, 2 (2008), 259–264.

[LSP03] LATSON L., SEBEK B., POWELL K. A.: Automated cell nuclear segmentation in color images of hematoxylin and eosin-stained breast biopsy. *Analytical and Quantitative Cytology and Histology 25*, 6 (2003), 321–331.

[MMVea13] MISTELBAUER G., MORAR A., VARCHOLA A., et al.: Vessel visualization using curvicircular feature aggregation. *Computer Graphics Forum 32*, 2 (2013), 231–240.

[MS93] MARKS J., SHIEBER S.: The Computational Complexity of Cartographic Label Placement. Tech. Rep. TR-05-91, Center for Research in Computing Technology, Harvard University, 1993.

[MSH*11] MATHEWS M. S., SU J., HEIDARI E., LEVY E., LINSKEY M. E., CHEN Z.: Neuroendovascular optical coherence tomography imaging and histological analysis. *Journal of Neurosurgery 69*, 2 (2011), 430–439.

[NDA*08] NAIK S., DOYLE S., AGNER S., MADABHUSHI A., FELDMAN M., TOMASZEWSKI J.: Automated gland and nuclei segmentation for grading of prostate and breast cancer histopathology. In *Proc. of IEEE Syposium on Biomedical Imaging (ISBI): From Nano to Macro* (2008), pp. 284–287.

[NGB*09] NEUGEBAUER M., GASTEIGER R., BEUING O., DIEHL V., SKALEJ M., PREIM B.: Map displays for the analysis of scalar data on cerebral aneurysm surfaces. *Computer Graphics Forum 28*, 3 (2009), 895–902.

[OP05] OELTZE S., PREIM B.: Visualization of vascular structures: Method, validation and evaluation. *IEEE Transactions on Medical Imaging 25*(4), 4 (2005), 540–549.

[Ots79] OTSU N.: An automatic threshold selection method based on discriminate and least squares criteria. *Denshi Tsushin Gakkai Ronbunshi 63*, (1979), 349–356.

[PM90] PERONA P., MALIK J.: Scale-space and edge detection using anisotropic diffusion. *IEEE Trans. Pattern Anal. Mach. Intell 12*, 7 (1990), 629–639.

[SCSG09] SERTEL O., CATALYUREK U. V., SHIMADA H., GURCAN M. N.: Computer-aided prognosis of neuroblastoma: Detection of mitosis and karyorrhexis cells in digitized histological images. In *Proc. of Conf. of IEEE Engineering in Medicine and Biology Society* (2009), pp. 1433–1436.

[TMF*12] TSAKANIKAS V. D., MAICHALIS L. K., FOTIADIS D. I., NAKA K. K., BOURANTAS C. V.: *Intravascular Imaging: Current Applications and Research Developments*. IGI Global, 2012.

[TSDS*11] TUNG K.-P., SHI W.-Z., SILVA R. DE, EDWARDS E., RUECKERT D.: Automatical vessel wall detection in intravascular coronary OCT. In *Proc. of IEEE Symp. on Biomedical Imaging: From Nano to Macro* (2011), pp. 610–613.

[Tul08] TULLEKEN H.: Poisson disk sampling. *Dev. Mag. 21*, (2008), 21–25.

[YKYea12] YOSHIMURA S., KAWASAKI M., YAMADA K., et al.: Visualization of internal carotid artery atherosclerotic plaques in symptomatic and asymptomatic patients: A comparison of optical coherence tomography and intravascular ultrasound. *American Journal of Neuroradiology 33*, 2 (2012), 308–313.

[ZMG*10] ZENG W., MARINO J., GURIJALA K. C., GU X., KAUFMAN A.: Supine and prone colon registration using quasi-conformal mapping. *IEEE Trans. Vis. Comput. Graph. 16*, 6 (2010), 1348–1357.

[Zui94] ZUIDERVELD K.: Contrast Limited Adaptive Histogram Equalization. In *Graphics gems IV*. Academic Press Professional, Inc., 1994, pp. 474–485.

[ZY14] ZENG W., YANG Y.-J.: Colon flattening by landmark-driven optimal quasiconformal mapping. In *Proc. of Medical Image Computing and Computer-Assisted Intervention (MICCAI)* (2014), pp. 244–251.

© 2016 The Authors
Computer Graphics Forum © 2016 The Eurographics Association and John Wiley & Sons Ltd.